



Seventh Framework Programme FP7-SPACE-2010-1  
 Stimulating the development of downstream GMES services

Grant agreement for: Collaborative Project. Small- or medium scale focused research project

Project acronym: **SIDARUS**

Project title: **Sea Ice Downstream services for Arctic and Antarctic Users and Stakeholders**

Grant agreement no. 262922

Start date of project: 01.01.11

Duration: 36 months

Project coordinator: Nansen Environmental and Remote Sensing Center, Bergen, Norway

## D5.5: SAR Image Analyses and Toolboxes

Due date of deliverable: 31.12.2013

Actual submission date: 20.01.2014

Organization name of lead contractor for this deliverable: AWI

Project co-funded by the European Commission within the Seventh Framework Programme, Theme 6 SPACE		
Dissemination Level		
PU	Public	X
PP	Restricted to other programme participants (including the Commission)	
RE	Restricted to a group specified by the consortium (including the Commission)	
CO	Confidential, only for members of the consortium (including the Commission)	

ISSUE	DATE	CHANGE RECORDS	AUTHOR
0	24/03/2011	Template	L.H. Pettersson
1.0	06/12/2013	Draft	Dierking et al.
2.0	15/01/2014	Final Version	Dierking et al.

### **SIDARUS CONSORTIUM**

Participant no.	Participant organisation name	Short name	Country
1 (Coordinator)	Nansen Environmental and Remote Sensing Center	NERSC	NO
2	Alfred-Wegener-Institut für Polar-und Meeresforschung	AWI	DE
3	Collecte Localisation Satellites SA	CLS	FR
4	University of Bremen, Institute of Environmental Physics	UB	DE
5	The Chancellor, Masters and Scholars of the University of Cambridge	UCAM	UK
6	Norwegian Meteorological Institute, Norwegian Ice Service	Met.no	NO
7	Scientific foundation Nansen International Environmental and Remote Sensing Centre	NIERSC	RU
8	B.I. Stepanov Institute of Physics of the National Academy of Sciences of Belarus	IPNASB	BR

No part of this work may be reproduced or used in any form or by any means (graphic, electronic, or mechanical including photocopying, recording, taping, or information storage and retrieval systems) without the written permission of the copyright owner(s) in accordance with the terms of the SIDARUS Consortium Agreement (EC Grant Agreement 262922).

All rights reserved.

This document may change without notice

## Table of Contents

<b>1 INTRODUCTION – CONTENTS OF THE REPORT .....</b>	<b>4</b>
<b>2 CLASSIFICATION OF SEA ICE .....</b>	<b>5</b>
N. ZAKHVATKINA AND E. SHALINA, NIERSC.....	5
2.1 INTRODUCTION .....	5
2.2 DATA.....	5
2.3 DATA PREPROCESSING .....	5
2.3.1 Calibration .....	5
2.3.2 Angular dependence correction.....	6
2.3.3 Noise reduction.....	6
2.3.4 Calculation and analysis of SAR Image Texture Features .....	7
2.4 DATA CLASSIFICATION .....	7
2.4.1 Support Vector Machines Classification technique.....	7
2.4.2 SAR data classification using SVM.....	9
2.4.3 Neural Network versus SVM.....	11
2.5 VALIDATION OF SVM CLASSIFICATION .....	12
2.6 REFERENCES.....	12
<b>3 ICEBERG DETECTION.....</b>	<b>14</b>
3.1 INTRODUCTION .....	14
3.2 ANALYSIS OF RESULTS IN ANTARCTICA FROM STANDARD ICEBERG DETECTION CHAIN .....	14
3.3 TOWARDS A NEW ICEBERG DETECTION MODULE.....	17
3.4 REFERENCES.....	20
<b>4 ICEBERG DRIFT AND DEFORMATION.....</b>	<b>21</b>
S. LINOW AND W. DIERKING, AWI .....	21
4.1 INTRODUCTION .....	21
4.2 CORRELATION FOR ESTIMATION OF ICE DISPLACEMENT.....	21
4.3 DEFORMATION.....	22
4.4 QUALITY ASSESSMENT .....	23
4.5 TECHNICAL OVERVIEW.....	25
4.6 RESULTS/PRODUCTS.....	26
4.6.1 Sea ice velocities.....	27
4.6.2 Drift vector reliability charts.....	27
4.6.3 Sea ice deformation determined from the displacement field .....	28
4.7 REFERENCES.....	28

## SUMMARY

In this report we describe the algorithms for retrieval of information about sea ice conditions that were developed or extended as part of the SIDARUS project. The algorithms are optimized for application on synthetic aperture radar (SAR) images. The information retrieval includes sea ice type classification, iceberg detection and tracking, and sea ice motion and deformation.

After the end of the Envisat mission, sea ice type and water separation is carried out using Radarsat-2 ScanSAR Wide Beam dual-polarization images. The polarizations are HH- and HV. The latter reveals noisy patterns that are removed before classification. The sea ice classification approach is based on the Support Vector Machines (SVM) approach, which is a supervised learning method. Besides radar intensities, eight textural parameters were selected as most informative parameters using statistical analysis. The texture characteristics considered are correlation, inertia, cluster prominence, energy, homogeneity, and entropy, as well as 3rd and 4th central statistical moments of image brightness. To include the effect of wind in the classification procedure, it is distinguished between calm and rough water surfaces. Sea ice classification results were compared with ice charts from the operational ice charting service (Met.no). The average difference is about 7 percent in winter and 11 percent in summer. The SVM-approach was also compared with the classification based on Neural Networks, showing that the former gave better results. The described procedure of RADARSAR-2 SAR image sea ice classification makes the base of the on-line service.

The detection of icebergs in SAR images is carried out in two steps: first a Constant False Alarm approach is used for identifying potential targets, followed by an automated rejection of false alarms based on criteria related to radiometric ambiguities. In the second step, a supervised selection is carried out using the targets remaining from step 1. This approach was used to support ship navigation in Antarctic waters during the Vendée Globe Challenge Yacht Race 2012/2013. The data were also employed to supplement former studies of the detectability of icebergs dependent on image properties and environmental conditions. It was found that the radar incidence angle and the wind speed did not affect the detectability in the 2012/2013 data, but it is assumed that this is an effect of an insufficient number of image acquisitions and iceberg detections. A new concept of iceberg detection is introduced, which is based on the Method of Moments and considers iceberg drift.

The retrieval of sea ice drift and deformation from SAR images is based on a cascaded multi-scale technique comprising phase correlation and normalized cross correlation. The algorithm for retrieving the displacement vector between the different positions of an ice surface structure that can be recognized in two images uses the input images processed at different spatial resolutions ("resolution pyramid"), gradually refining the resulting drift field ("cascade"). Deformation parameters are calculated using the drift field as input. A major challenge is to provide information on the reliability of the drift field. A robust possibility to achieve this is to carry out the calculations two times, the second time using image #2 as starting point (backmatching). This approach, however, doubles the computation time. Therefore, another measure is introduced that combines the analysis of textural and correlation parameters in a confidence factor (CFA).

# 1 Introduction – Contents of the Report

This report is the Deliverable 5.5 of WP 5. It is related the applications of the toolbox modules that are introduced in report 5.4. The algorithms on which the toolbox modules are based are presented together with results from a number of tests. Information on achievable accuracies or on methods for judging the reliability of the results is provided.

The report covers the following topics:

- (1) sea ice classification (main responsibility NERSC and NIERSC, see section 2)
- (2) iceberg detection and tracking (main responsibility CLS, see section 3)
- (3) monitoring of sea ice drift and deformation (main responsibility AWI, see section 4)

## 2 Classification of Sea Ice

N. Zakhvatkina and E. Shalina, NIERSC

### 2.1 Introduction

Previous reports (deliverables 5.1 and 5.3) described sea ice classification methods that were specifically tuned for and applied to ENVISAT SAR data. Since in 2012 ESA announced the end of the ENVISAT mission it has become very important to develop an automatic ice classification method for other available SAR systems. Over the last several months NIERSC has worked on designing and establishing a new automatic algorithm to process RADARSAT-2 data.

### 2.2 Data

RADARSAT-2 is a Canadian Earth observation satellite that was launched in December 2007. Its capabilities that benefit sea-ice applications are the multi-polarization options that improve ice-edge detection, ice-type discrimination, ice topography and structure information.

The satellite carries a Synthetic Aperture Radar (SAR) with multiple polarization modes, including a fully polarimetric mode in which HH, HV, VV and VH polarized data are acquired. RADARSAT-2 products are characterized by the beam mode used by the satellite and the level of processing that has been applied to the data.

Its highest resolution is 1 m in Spotlight mode (3 m in Ultra Fine mode) with 100 m positional accuracy requirement. The ScanSAR mode provides images of very wide swaths in a single pass of the satellite, and is intended for use in applications requiring large-scale area coverage such as monitoring applications.

In our study we work with data received in ScanSAR Wide Beam (SCW) mode. ScanSAR images can be generated either with a single linear co-polarization, or with a single linear cross-polarization, or with dual co- and cross-polarizations. Our algorithm is developed for images of HH and HV polarization, for data that has a nominal swath width of 500 km and a pixel spacing 50 m × 50 m.

### 2.3 Data Preprocessing

#### 2.3.1 Calibration

Calibration of the backscatter values to  $\sigma^0$  was done using the following formula

$$\sigma_i^0 = A_i^2 / K \cdot \sin(\alpha_i), \quad (1)$$

where: K - absolute calibration constant, i - pixel number,  $A_i^2$  - average pixel brightness,  $\alpha_i$  - incidence angle for each pixel.

Radiometric calibration is applied on the radar imagery to get the actual representation of the radar backscatter. Below some characteristics of data of different polarization are discussed. The HV channel-SAR image always appears darker than the HH channel because the backscatter is always lower in HV. This is because the SAR transmits horizontally polarized impulses, so that there is a tendency to scatter backwards predominantly H-polarization (seen in HH) rather than V-polarization (seen in HV). First year ice is bright in both HH and HV while gray ice type is darker. New ice and open water are very similar, appearing bright in HH and dark in HV. However, open water tends to be smoother with no visible structures. Smooth forms of gray ice, new ice and water are all dark in both HH and HV bands. Ice floes on the first year ice are very well defined in

the HV image. Wind roughened water or new ice are difficult to distinguish from the first year ice in the HH band alone at small incidence angles. The HV band, however, provides information on the location of the first year ice since water and new ice are dark. Dual-polarization ENVISAT ASAR data, which was similar to RADARSAT-2 data, was analyzed and tested for its ability to discriminate sea ice types.

### 2.3.2 Angular dependence correction

In order to classify SAR images where  $\sigma^{\circ}$  is a function of incidence angle, the  $\sigma^{\circ}$  values are normalized across the swath, using  $35^{\circ}$  as a reference angle and a linear function for predominant ice type. Although the difference in radar backscatter between different ice types is slightly higher at far range of SAR image, we used  $35^{\circ}$  angle, which allows analyzing SAR image without brightness amplification. The predominant ice type is identified by means of SAR image visual inspection. The normalization method consists of two stages: calculation of the backscatter coefficient using image brightness according to the formula (1) and backscatter recalculation to  $35^{\circ}$  incidence angle using developed procedure. The backscatter normalization to pre-defined incidence angle allows obtaining homogenous image contrast across the swath. The incidence angle of  $35^{\circ}$  provides a satisfactory contrast between various ice types.

### 2.3.3 Noise reduction

The low radar backscatter values of the cross (HV) polarization are sometimes below the system noise floor and result in brighter/darker striping in the along-track direction. The reason why these artifacts arise is that the ScanSAR Wide Beam mode assembles wide SAR image from several narrower SAR beams and those beams have different noise levels. The artifacts are most noticeable at the beam boundaries. This effect is reduced by subtracting the expected noise floor level from the image values. Unfortunately the procedure does not work always perfectly and sometimes the noise cannot be completely removed. The illustration of noise impact and noise reduction is shown in Fig.2.1. The left image is the raw HV channel image, and the right one is the noise reduced image. The graph below images illustrates the process of noise subtraction. The blue curve shows the  $\sigma_0$  value profile of the raw HV channel image over the horizontal line, the red curve depicts the noise floor level and the green curve is the result of subtraction.

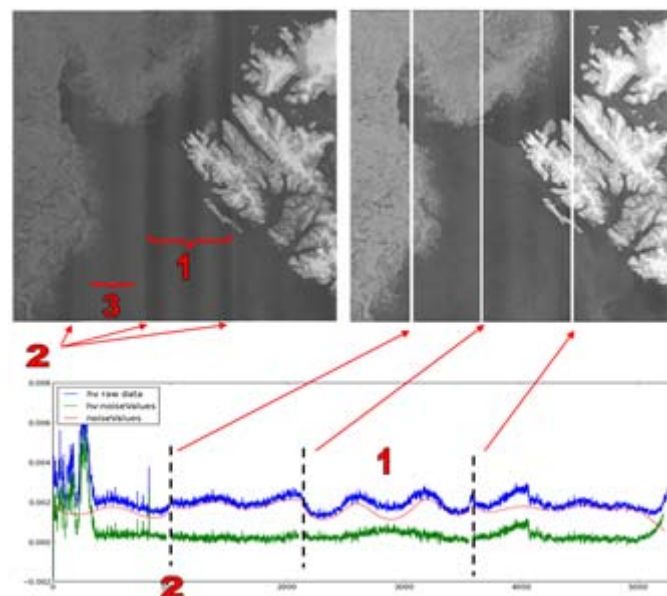


*Fig. 2.1. Noise effects and noise reduction in HV polarization image. 1) Visible noise floor variations; 2) beam boundaries are visible due to differences in noise levels between adjacent beams; 3) the image appears brighter in the beam W30 due to higher noise levels in that beam.*

The procedure of noise reduction consists of two steps: 1) extracting noise values from metadata RADARSAT-2 xml file and 2) subtracting noise values from the raw HV channel-SAR image.

Since a single noise profile is provided in the metadata and its impact on the image shifts along the azimuth direction, there could be problems with representation of actual backscatter behavior. Also due to the sub-beam stitching in ScanSAR processing, adjusting the signal level in the post-processing introduces issues at the beam boundaries (see Fig.2.1).

### 2.3.4 Calculation and analysis of SAR Image Texture Features

Several studies have shown that SAR sea ice classification accuracy is improved by using image texture features (Hara et al., 1994; Bogdanov et al., 2005; Haarpainter J., 2007). Texture depends on the spatial scale of sea ice surface and volume inhomogeneity, as well as on radar spatial resolution. Texture features describe spatial variations of image brightness within a group of neighbour pixels large enough to calculate statistically significant estimates. A given texture feature can be different from one ice type to another and reflect variability in sea ice properties sensed by the SAR.

After  $\sigma^0$  normalization to  $35^\circ$  incidence angle eight texture features - correlation, inertia, cluster prominence, energy, homogeneity, and entropy have been calculated in the study. This has been done for a set of images representing relatively homogeneous areas of different ice types (Zakhvatkina et al., 2012). The normalized texture value for each texture feature and ice type has been calculated for four window sizes (16, 32, 64, and 128 pixels). Visual examination of mean texture values suggested that the  $32 \times 32$  sliding window provides better separation of the ice types compared to other window sizes. Analysis of texture characteristics' classification efficiency revealed, for example, that the cluster prominence versus energy and correlation versus energy provide good separation between level first-year ice, deformed first-year ice and multiyear ice. Separation of open water and nilas can be done by use of cluster prominence versus energy and to some degree by inertia/contrast versus energy.

Statistical analysis showed that the entire set of selected texture features can be used for discrimination of the four ice types. Therefore, all eight texture features and the backscatter coefficients have been used as input for training and classification of sea ice types in the Arctic.

## 2.4 Data Classification

Working with ENVISAT SAR data we based on Neural Network technique in data classification. After switching to RADARSAT data the study has been carried out to find the best procedure for data classification. It was found that Support Vector Machines method provides the best results.

### 2.4.1 Support Vector Machines Classification technique

The support vector machines (SVM, also called support vector networks) are supervised learning methods with associated learning algorithms that provide data classification. The basic SVM takes a set of input data and predicts, for each given input, which of two possible classes forms the output, making it a non-probabilistic binary linear classifier. The divided into classes objects are mapped so that the examples of the separate categories are separated by a clear gap that is as wide as possible. SVM can also perform a non-linear classification using what is called the kernel trick, implicitly mapping their inputs into high-dimensional feature spaces. A special property of the SVMs is that they simultaneously minimize the empirical classification error and maximize the geometric margin; hence they are also known as maximum margin classifiers (Fig. 2.2). The distance between the lines that separate classes is called the margin. The vectors (points) that constrain the width of the margin are the support vectors.

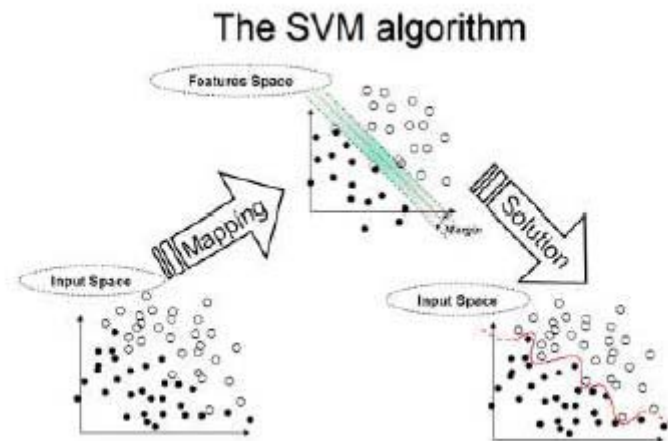


*Fig. 2.2. Overview of the SVM process.*

The simplest way to divide two groups is with a straight line, flat plane or an N-dimensional hyperplane. In case when the features can be separated only by a nonlinear boundary, rather than fitting nonlinear curves to the data, SVM handles this by using a kernel function to map the data into a different space where a hyperplane can be used to do the separation (Fig. 2.3).

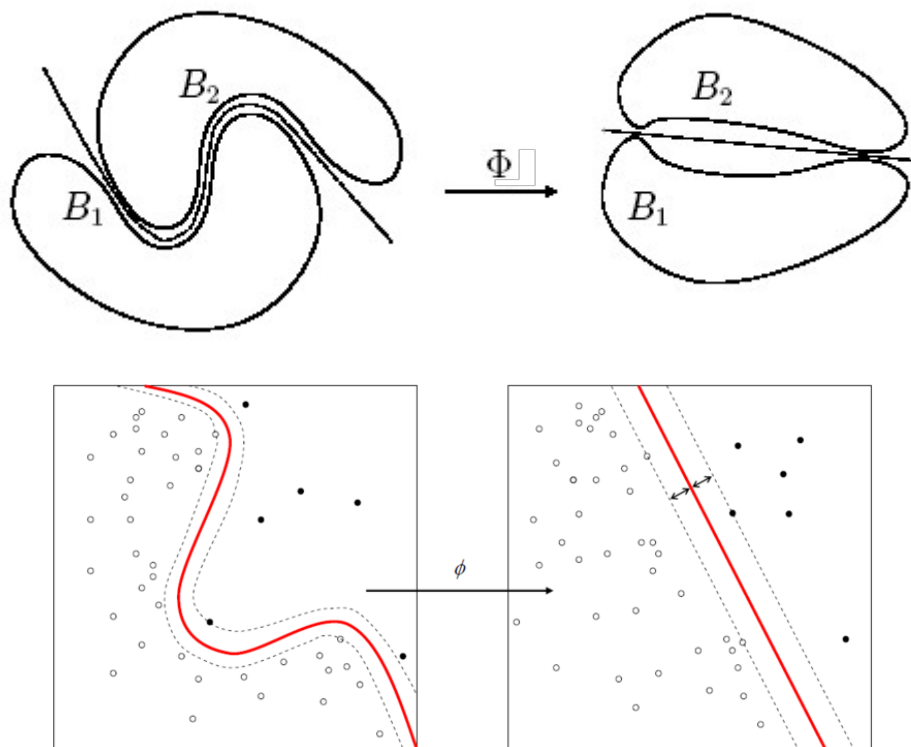


*Fig. 2.3. Applying kernel function  $\Phi$  (kernel function mapping) in SVM algorithm.*

The kernel function may transform the data into a higher dimensional space to make it possible to perform the separation. In our study we have used the radial basis function kernel, or RBF kernel, which is found to work well in a wide variety of applications. It uses squared Euclidean distance between the two feature vectors and can be interpreted as a similarity measure.

The confirmed advantages of support vector machines method are:

- The method is effective in high dimensional spaces.
- It is also effective in cases where number of dimensions is greater than the number of samples.
- Uses a subset of training points in the decision function (as support vectors), which means it is memory efficient.
- The method is adaptable: different *kernel functions* can be specified for the decision function.

#### 2.4.2 SAR data classification using SVM

The procedure of SVM tuning (learning) in our case involves the following steps:

1. A series of 16 RADARSAT-2 ScanSAR images (pixel spacing 50 m × 50 m, 500 km swath width) at HH- and HV-polarizations, acquired over Fram Strait in winters of 2011 and 2012 were used for analysis of the sea ice and water backscatter  $\sigma_0$ .
2. The backscatter coefficients for ice and water were derived after special noise correction of HV-polarization image.
3. After noise correction and  $\sigma_0$  calculation eight texture characteristics - correlation, inertia, cluster prominence, energy, homogeneity, and entropy, as well as 3rd and 4th central statistical moments of image brightness have been calculated for both – HH- and HV- polarizations (Total = 18, i.e. textural characteristics +  $\sigma_0$  of HH and HV). Six textural features were selected using statistical analysis as most informative parameters. They have been used further in algorithm completion.
4. The expert analysis of RADARSAT-2 ScanSAR images was done to delineate sea ice (2 ice types) and open water (calm and rough open water). We also applied the K-means classification method to get an automatic segmentation of SAR images (classification generated 6 classes). Then these two results were compared to get a number of training vectors (supervised training dataset) for SVMs tuning as inputs.
5. Selected dataset was applied for SVM training. We decided to have 2 ice types and 4 types of different open water (the decision was affected by comparison of expert visual estimation and K-means segmentation).

The process of SVM training is illustrated by Fig. 2.4.

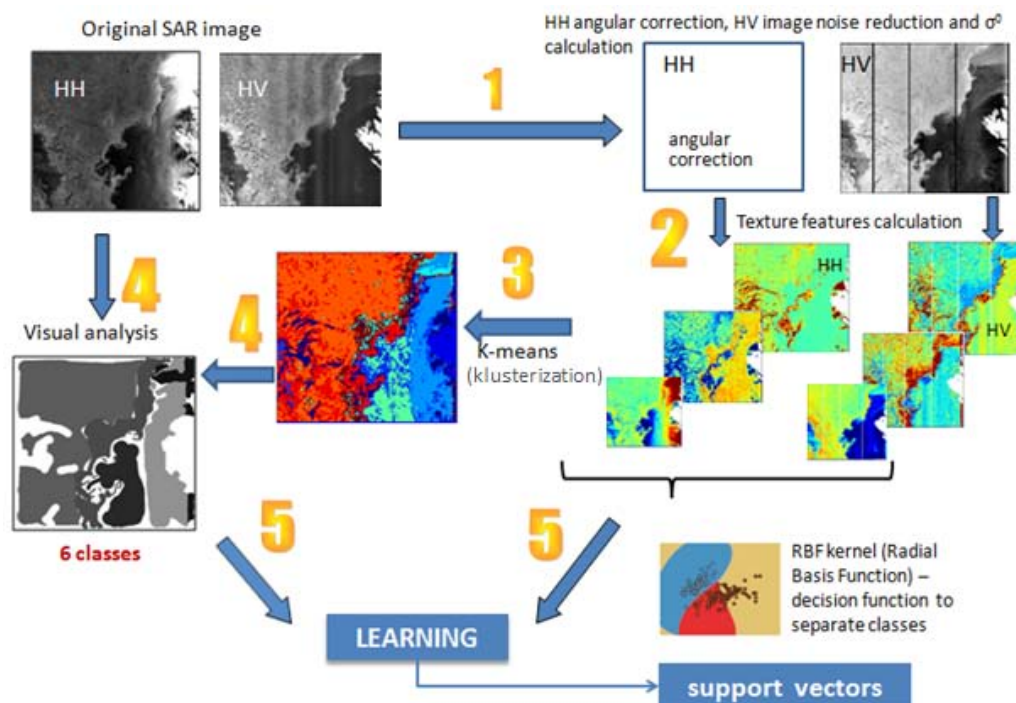


Fig. 2.4. SVM learning before using it for sea ice classification.

After tuning has been done SVM is ready for sea ice classification. The classification process was described in report 5.4 but is repeated here for the ease of reference. It contains the following stages:

1. RADARSAT-2 raw data preprocessing. The stage includes backscatter coefficients calculation and noise correction of HV- polarization image.
2. Textural characteristics calculation. The set of textural features (which characteristics have to be calculated is determined early during SVM tuning) and sigma0 for HH- and HV-polarizations make the basic data for classification.
3. SVM classification. The result is several classes of ice and water.
4. Reclassification of SVM results in order to have only three classes – open water calm, open water rough and the sea ice.

SVM classification procedure is illustrated by Fig. 2.5.

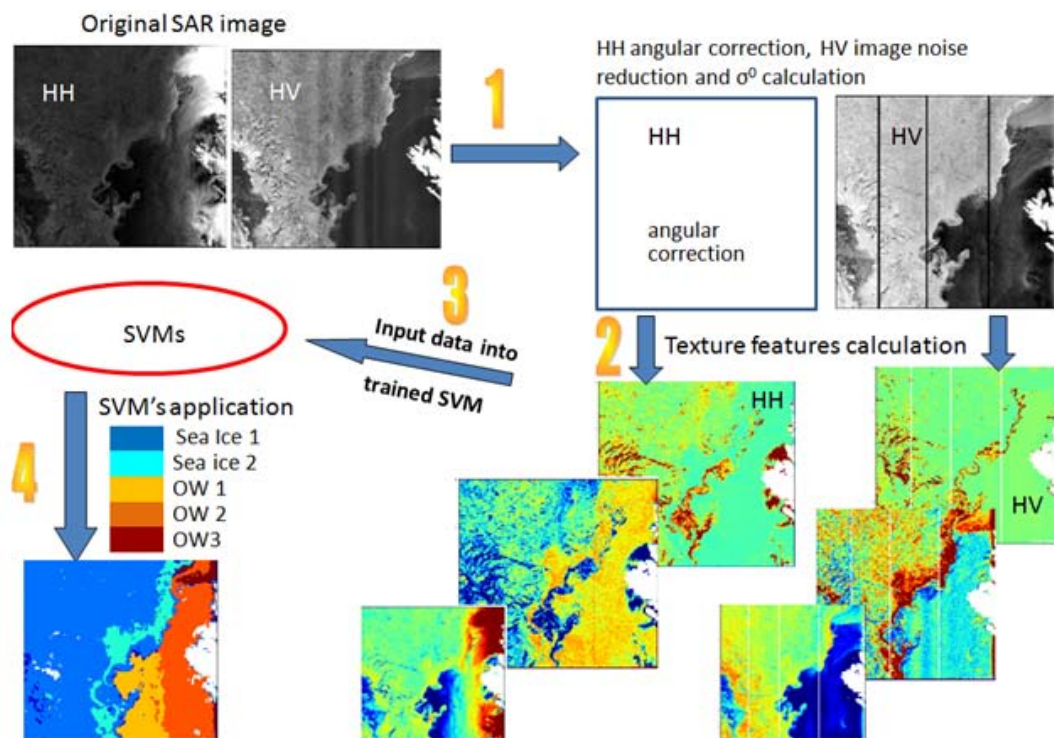


Fig. 2.5. SVM classification procedure.

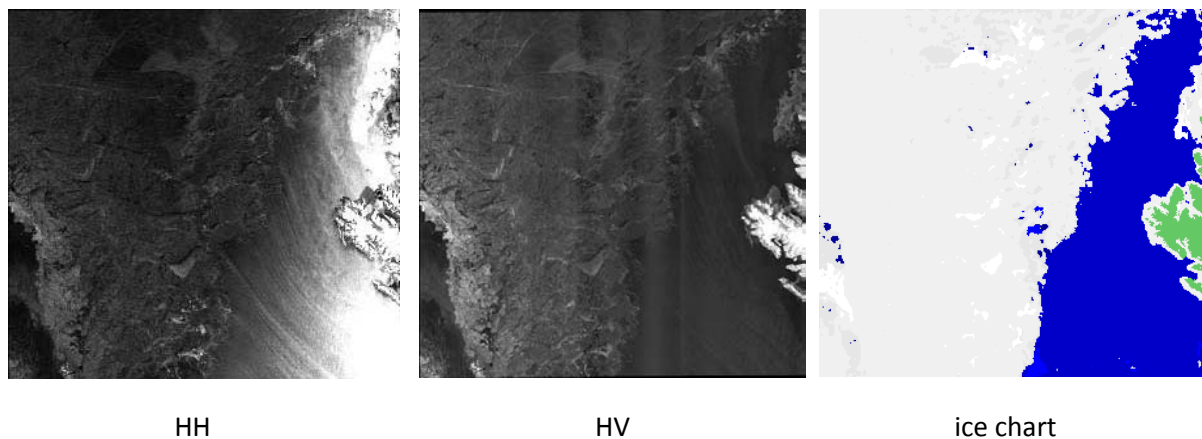


Fig. 2.6. SVM classification result.

The example of automatic SVM classification based on two (HH and HV) channels of RADARSAT-2 SAR image is shown in Fig. 2.6. The image has been taken on March 7, 2013, it shows the region in the Fram Strait. In the ice chart the sea ice is colored in grey, water is colored in blue, and the land is shown in green. The darker feature at the left-hand side of each image is a pack ice near Greenland.

### 2.4.3 Neural Network versus SVM

Before choosing SVM technique as a base method for RADARSAT-2 SAR data classification we tried to apply Neural Network (NN) algorithm in the process of RADARSAT-2 automated classification (Zakhvatkina et al., 2012). Comparison of the NN-algorithm classification results with a SVM's shows that SVM in our case provides better results (see Fig. 2.7).

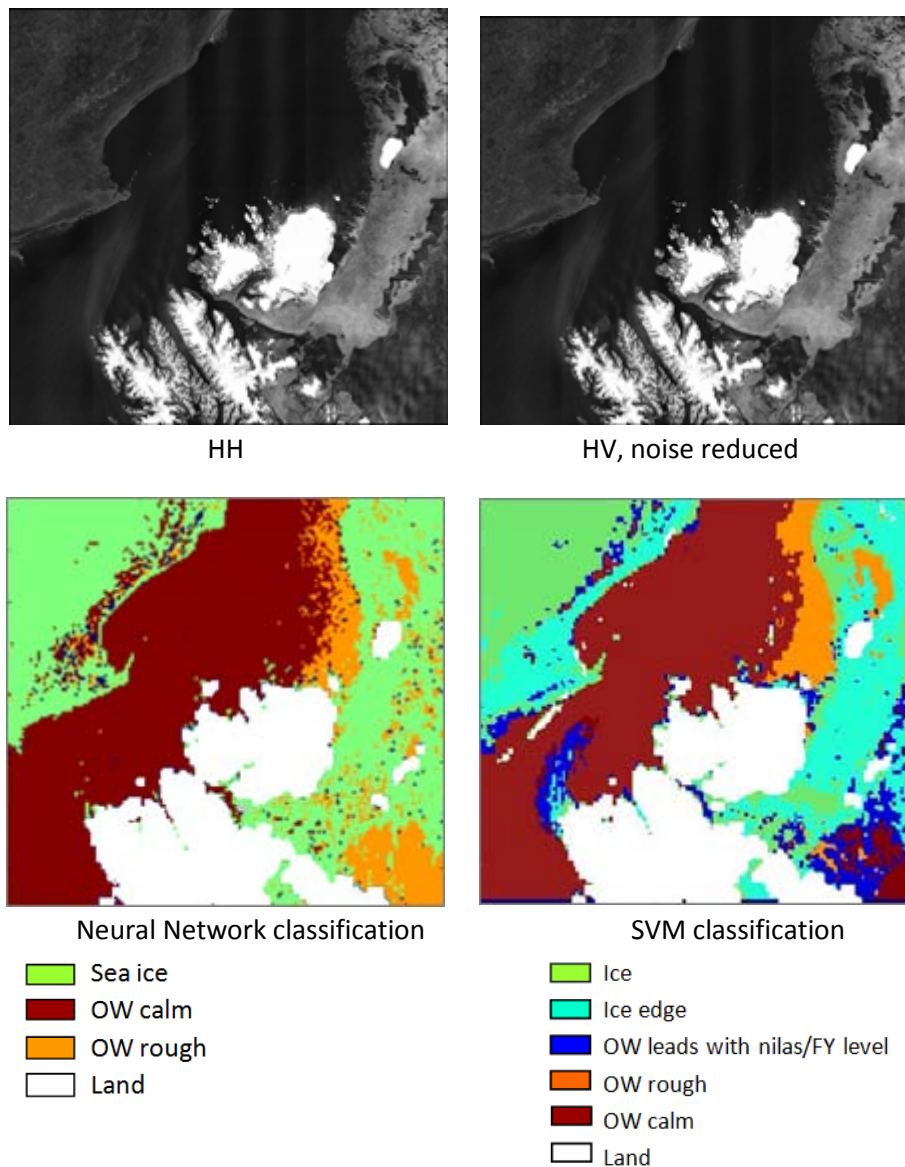


Fig. 2.7. Comparison of the NN- and SVM classification results.

SVM's classification of the ice age area is more accurate than NN's. The broken ice is classified as ice by SVM algorithm but often classified as rough water by NN. SVM's classification of water is also more accurate. In case of NN algorithm more water pixels are erroneously classified as ice. Leads

with water are usually classified as first year ice by NN algorithm, while they are classified as open water by SVM. We also have found that SVM is less sensitive to remained noise.

## 2.5 Validation of SVM classification

Sea ice classification results calculated using SVMs technique have been intercompared with Met.no ice charts from the operational ice charting service. Validation of Arctic ice products is always a challenging task due to lack of ground truth data. As a substitute, our product has been intercompared with a manual sea ice product produced by Met.no.

Met.no ice charts are produced by ice analysts at the Norwegian Sea Ice Service using the following data sources: high resolution microwave Synthetic Aperture Radar data (Radarsat), low resolution microwave SSM/I and SSMIS data (DMSP), MODIS data (Terra and Aqua) and AVHRR data from NOAA. The example of comparison is shown in Fig. 2.8.

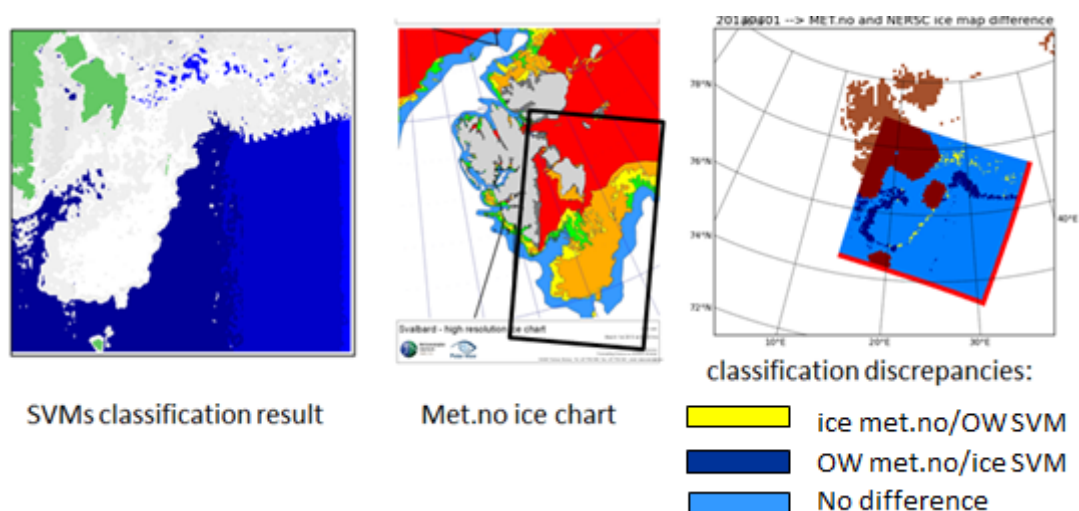


Fig. 2.8. Intercomparison of METNO and SVM ice charts for 01 March 2013.

Overall accuracies for the period March-October 2013 are shown in the table below. The accuracy values are derived using the assumption that Met.no ice charts represent correct classification. Validation is discussed in more detail in 8.3 report.

month	Mar	apr	May	jun	jul	aug	sep	oct
<b>Overall accuracy</b>	0,92	0,92	0,89	0,87	0,81	0,86	0,88	0,94

## 2.6 References

Bogdanov A., S. Sandven, O. M. Johannessen, V. Alexandrov, and L. Bobylev, Multisensor Approach to Automated Classification of Sea Ice, IEEE Trans. Geosci. Remote Sens., vol. 43, no 7, pp. 1648–1664, Jul. 2005.

Haarpaintner J., Solbo S. Automatic ice-ocean discrimination in SAR imagery-2007. NORUT– report 06/2007, pp. 28, 2007.

Hara Y., R. G. Atkins, R. T. Shin, J. A. Kong, S. H. Yueh, and R. Kwok, Application of Neural Networks to Radar Image Classification, IEEE Trans. Geosci. Remote Sens., vol. 32, no 1, pp. 100–109, Jan. 1994.

Zakhvatkina N., V. Alexandrov, O.M. Johannessen, S. Sandven, I. Frolov. Classification of sea ice types in ENVISAT synthetic aperture radar images. IEEE Transactions on Geoscience and Remote Sensing, 10.1109/TGRS. 2012. 2212445. vol.51, issue 5, pp. 2587-2600.

## 3 Iceberg Detection

N. Longép  and R. Pelich, CLS

### 3.1 Introduction

Synthetic Aperture Radar (SAR) imagery is a key earth observation tool to monitor ice phenomena, as radars are independent on day/night cycles as well as cloud conditions. SAR technology can be used to deliver an integrated iceberg surveillance service for maritime security (e.g. world sailing race such as the Vend e Globe in the South Atlantic seas). The service is based on a two steps approach with a first phase of integration of an observation/detection using satellite SAR imagery with met-ocean data and competitors positions, followed by a second phase of drift modelling.

Beyond swell, current and wave monitoring, two modules of the SARTool software were used for the demonstrations. The first one, "SARTool ship", is dedicated to echo detection (iceberg and vessels). The second one, "SARTool annotation", has a specific GUI enabling a supervised selection of target type within SAR images.

Here are some details about the chain:

- ✓ Firstly, an automatic detection is operated using the "SARTool ship" module. This algorithm basically runs as follows:
  - Region of interest selection and land mask application
  - Detection using a CFAR approach (Constant False Alarm Rate)
  - Rejection of false alarms corresponding to radiometric ambiguities (weak target...), azimuthal and nadir ambiguities.
- ✓ The output of this step consists in a list of potential targets. Each of them is qualified as "reliable" or "unreliable" depending on the rejection step. In addition to this, the length of each target is estimated using an "image-based" approach.

In the frame of SIDARUS project, several modifications have been implemented and tested. As mentioned in the deliverable D5.4, a new approach based on Neural-Network has been already tested and partially validated with iceberg in sea ice in the Arctic Seas. In addition, the "SARTOOL annotation" module has been upgraded to enable a much faster interface for data and iceberg products handling and visualization.

In this section, new perspectives for iceberg detection based on new detectors (not only CFAR but also non-parametric detector) are outlined and the results from the past Vend e Globe Challenge 2012 (round-the-world single-handed yacht race) with standard detection chain are analyzed.

### 3.2 Analysis of results in Antarctica from standard iceberg detection chain

For the demonstration during the last Vend e Globe of the winter 2012-2013, SAR images acquired by the Radarsat-2 satellite was used (see Fig. 3.1). In order to maximize the coverage of the monitored areas, most of SAR images were acquired in ScanSAR Wide swath mode, with coverage of 500 km x 500 km per scene. In this report, some analysis of the results from this demonstration is

carried out. At this stage, it should be noted that supervised-echo-qualification is integrated in the processing chain.

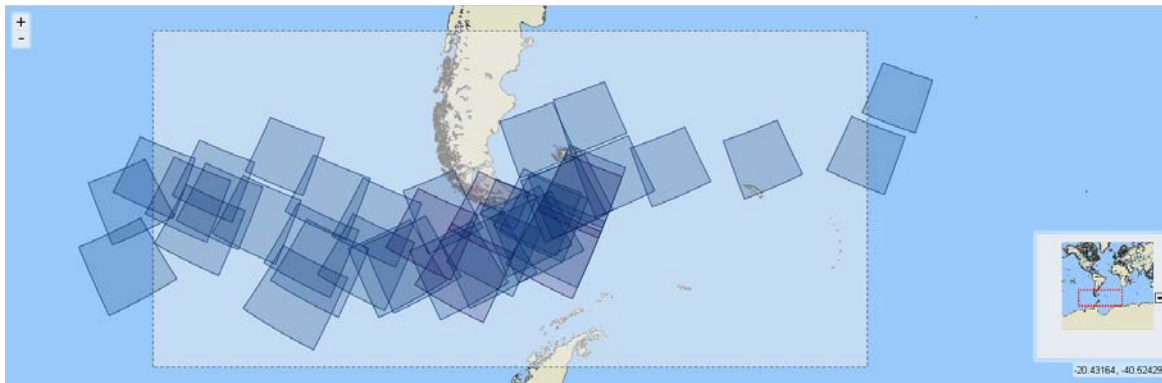


Figure 3.1 Frames of image acquired for VG 2012 nearby the Cape Horn

In the following analysis, we used more than 150 HH RS2 ScanSAR Wide images, from where 350 icebergs were detected. The following Figures 3.2 and 3.3 show examples of the information, which is provided by the software tool to support an analysis of the number of detected qualified echoes with respect to observation condition (local incidence angle and wind speed).

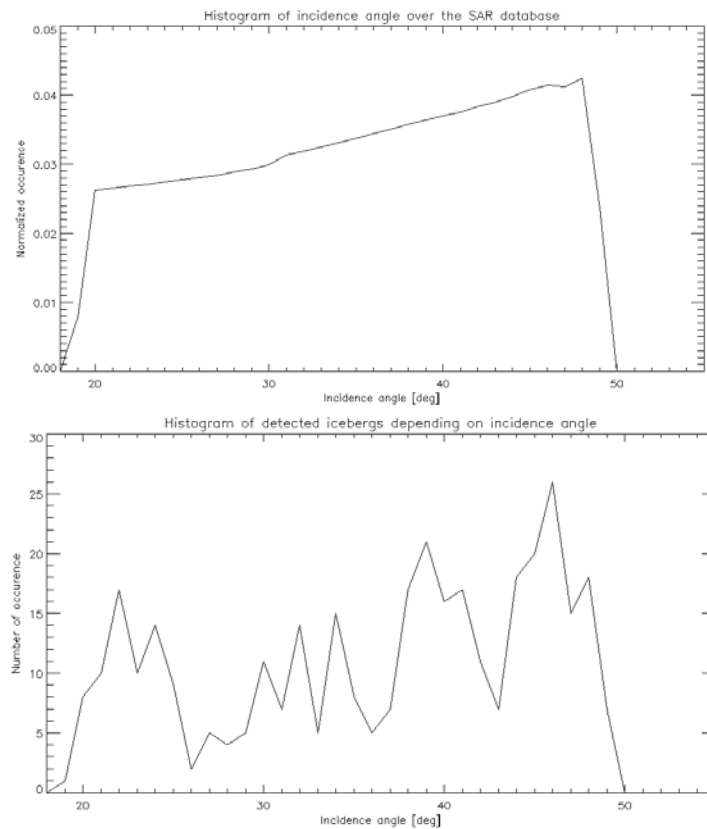


Figure 3.2 Incidence angle range from the dataset (Top) and histogram of detected icebergs with respect to incidence angle (Bottom)

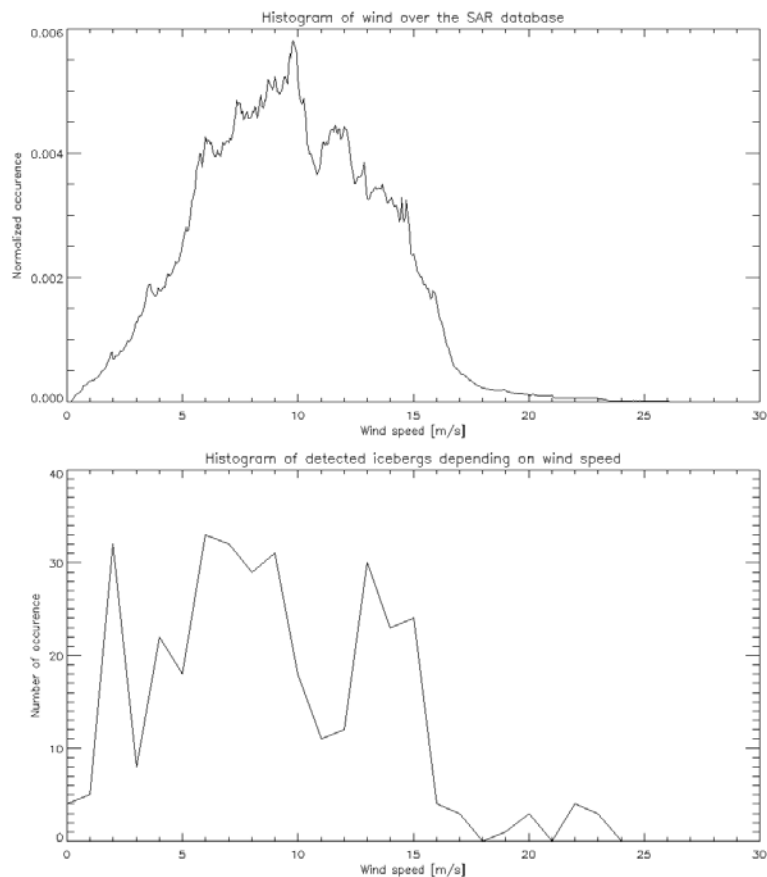


Figure 3.3 Wind speed range from the dataset – source ECMWF (Top) and Histogram of detected icebergs with respect to wind speed (Bottom)

From the above figures, no clear conclusion can be outlined (up to now):

- the incidence angle does not seem to impact the detectability of icebergs over our dataset with RS2 ScanSAR wide images
- Same conclusion for wind speed.

Two main reasons explain these results:

- As compared to the analysis of D5.1 with WSM/ASAR data from VG2008, the number of acquisitions and detected icebergs for the last VG2012 is not sufficient to assess quantitatively the detectability of iceberg with respect to wind speed and/or incidence angle. In the VG2008, the acquired ENVISAT images were long stripes with coverage up to the Antarctica shelf. For the last edition, we focused on the routes foreseen by the sailboat, with acquisitions generally above 57°S (except nearby CapeHorn), thus reducing the overall covered area. No area with high concentrated icebergs has been detected, thus highly reducing the number of reference echoes.
- Out of the small number of detections, a large part of icebergs greater than 200 meters (4 x ScanSAR pixel spacing) has been detected during the VG2012 (see Figure 3.4). For large icebergs, the pros and cons of CFAR algorithms are negligible, and icebergs are easily detected with visual human supervision. In this particular case, the contrast between the NRCS of icebergs and its surrounding clutter is not fundamental: no correlation with wind speed and incidence angle is then found.

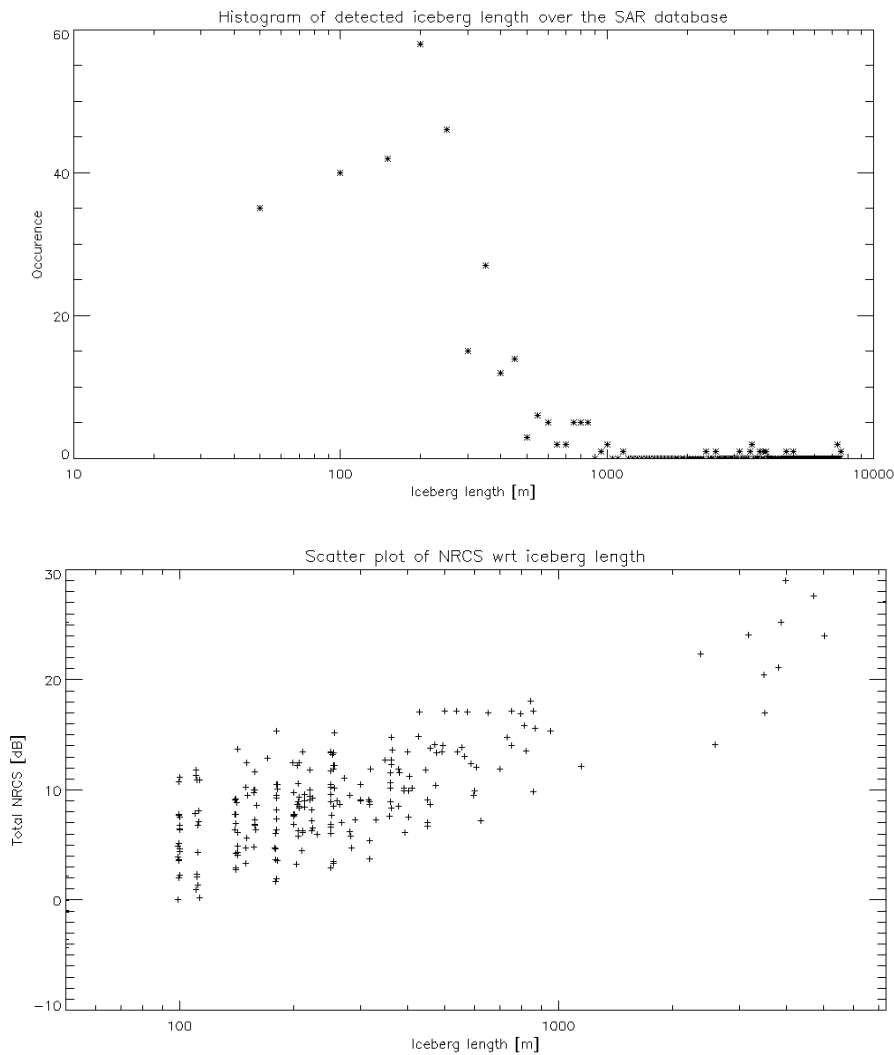


Figure 3.4 Histogram of the length of detected icebergs from the last VG2012 demonstration (Top) and Scatter plot of the total NRCS of iceberg depending on their length (Bottom).

### 3.3 Towards a new iceberg detection module

In this subsection, some tests for a new iceberg detection scheme have been initiated. In particular, a new approach based on a non-parametric detector has been tested.

The following briefly describes the detection algorithms. The CFAR detector is very often used in ship-iceberg detection and many papers have already treated the subject. (Crisp et al. 2004) give a very good synthesis of existing papers. We remind that designing an adaptive threshold algorithm (CFAR in our case) implies to compare the possible targets within a sliding window (pixels under test  $x_{\text{test}}$ ) to a threshold depending on the statistics of the surrounding area (background cell  $x_B$ , a buffer area being used). In order to compute the threshold, statistics in the background cell and the corresponding probability density function (PDF) for a desired probability of false alarm (PFA) need to be estimated.

Two classical methods for estimating parameters of statistical distributions are the Method of Moments (MoM) and the Maximum Likelihood Estimation (MLE). In this study, the MoM has been used and the corresponding statistical parameters of the background area are the mean,  $\mu_B$ , and the standard deviation,  $\sigma_B$ . Various statistical models can be considered: the Gaussian distribution, the

Gamma distribution or the K-distribution. In this study, the Gamma distribution is used as multi-look SAR images supposedly follow this distribution. For this detector, the order parameter  $L$  should be computed. We can use for  $L$  either the number of looks given in the sensors documentation, or estimate it from the background statistics (equivalent number of looks (ENL) defined by:  $(\mu_B / \sigma_B)^2$ ).

For the detectors based on the non-parametric approach (see Atto 2008), the following hypothesis are considered:

$$\begin{cases} H_0 : Y \sim N(0, \sigma^2) \\ H_1 : Y = S + X, \lambda_u \leq |S|, X \sim N(0, \sigma^2) \end{cases}$$

where  $X$  and  $S$  are independent,  $S$  being a signal of unknown distribution (in our case  $S$  represents the targets and  $X$  the background). Assuming that  $S$  is of very small dimensions compared to  $X$  (number of samples), according to theory, the maximum of  $X$  has a strong probability of being close to  $\lambda_u$ . The  $\lambda_u = \sigma\sqrt{2\ln(N)}$  is the so-called universal threshold (Donoho, 1995). We assume that the probability of occurrence of  $H_1$  is less than a certain  $p$  ( $<0.5$ ). Under all these assumptions a non-parametric threshold,  $\lambda_n$ , representing a lower-bound for  $|S|$ , is defined as (Atto 2008):

$$\lambda_n = \sigma\xi\left(\frac{\lambda_u}{\sigma}, p\right) \quad \xi(a, p) = \frac{a}{2} + \frac{1}{a} \left[ \ln \frac{1-p}{p} + \ln \left( 1 + \sqrt{1 - \frac{p^2}{(1-p)^2} e^{-a^2}} \right) \right]$$

Finding  $\lambda_u$  or  $\lambda_n$  implies the estimation of  $\sigma$  which is the standard deviation of the background, in our case. Since we use intensity images, the assumption  $X \sim N(0, \sigma^2)$  will not be valid. But multi-look SAR intensity images are the sum of  $L$  terms ( $I_L^2 + Q_L^2$ ), where  $I_L$  and  $Q_L$  represent the real and imaginary components of radar scatter for each look. Because  $I_L$  and  $Q_L$  are independently Gaussian distributed, we can easily find a relationship between  $\sigma_{I/Q}$  and  $\sigma_{intensity}$  (which could be estimated) and inject  $\sigma_{I/Q}$  for finding  $\lambda_u$  or  $\lambda_n$ . More information will be available in (Pelich et al. 2014).

The comparison of results between the two detectors is shown in the following figures.



Figure 3.5 ScanSAR RS2 image acquired on 2013/12/03 over Franz Joseph

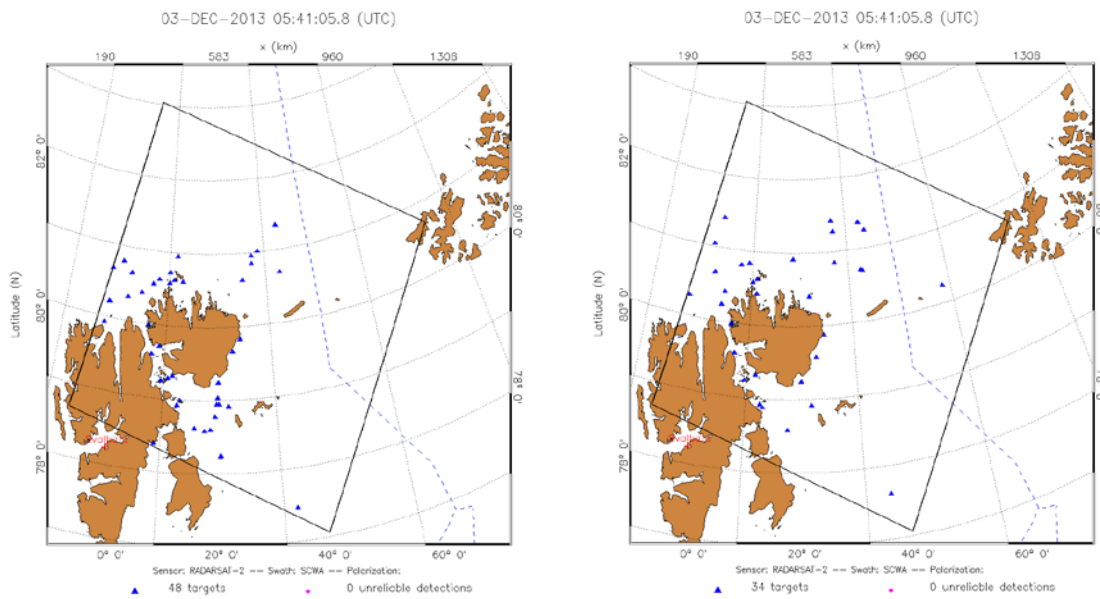


Figure 3.6 Bright target detection with the non-parametric detector with  $p=0.01\%$  (Left) and the CFAR detector with Gamma assumption and  $PFA=10^{-16}$  (Right) – Warning: no post-qualification is operated here !!!

As the processes for bright target detection are different (one is based on a Prior False Alarm Probability with Gamma distribution and the other is based on the probability of occurrence of signal in Gaussian noise), the detected bright echoes are sometimes not similar (as shown in the above figure). Here it should be noted that the number of detected bright echoes is way too high compared to the expected number of icebergs in December over this area. The detection scheme should absolutely be followed by a qualification step with rejection of false alarms (see deliverable D5.3). Advanced integration of AIS (Automatic Identification System) data flows for vessel/iceberg discrimination will have to be carried out as well.

A perspective to this subsection will be to constrain the detection scheme by the expected rate of icebergs in a given area. In order to perform this task, we plan to further integrate the drift simulation shown in Figure 3.7.

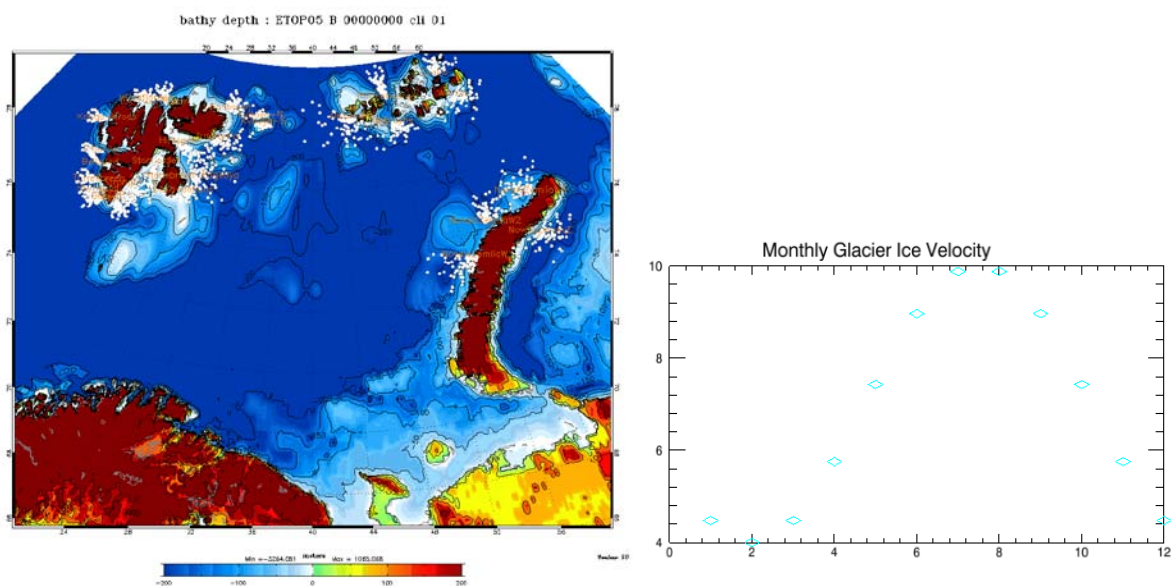


Figure 3.7 : Iceberg generation for a 14-day period (Left) depending on the monthly glacier flow rate (Right)

In addition to the aforementioned perspectives with advanced echo-qualification with the Neural Network method and AIS integration, an advanced algorithm for ice and iceberg segmentation will be soon introduced. The MDL polygonal grid segmentation for complex Arctic environment has been described in the deliverable D5.3. With the upcoming of high-resolution large-swath SAR sensors, the identification of icebergs will pose new issues in the Arctic Sea. Especially, the larger icebergs will be imaged by several pixels whose backscattering may be potentially within the backscattering level of surrounding ice. Segmentation and identification of groups of pixels should be foreseen within the iceberg detection chain.

### 3.4 References

A. M. Atto, D. Pastor, and G. Mercier, "Detection thresholds for nonparametric estimation," *Signal, Image and Video Processing Springer*, vol. 2, no. 3, pp. 207–223, 2008.

David L. Donoho, "De-noising by soft-thresholding," *IEEE TRANSACTIONS ON INFORMATION THEORY*, vol. 41, no. 3, pp. 613–627, May 1995.

D. J. Crisp, "The state-of-the-art in ship detection in synthetic aperture radar imagery," *Intelligence, Surveillance and Reconnaissance Division Information Sciences Laboratory, Edinburgh, South Australia, Australia, Tech. Rep.*, May 2004.

Pelich R., Longepe N. , Mercier G., Hajduch G., and R. Garello, " AIS-based Evaluation of Target Detectors and SAR Sensors Characteristics for Maritime Surveillance", Submitted to *IEEE JSTARS*, Jan. 2014.

## 4 Sea Ice Drift And Deformation

S. Linow and W. Dierking, AWI

### 4.1 Introduction

Sea ice drift and deformation is obtained for the overlap area of a pair of SAR images acquired at two different times. The algorithm for retrieving the displacement vector (i. e. distance and direction) between the changing positions of an ice surface structure that can be recognized in both images is based on a correlation technique, using the input images processed at different spatial resolutions, gradually refining the resulting drift field (cascaded resolution pyramids). The ice displacements retrieved from sequences of SAR images reflect position changes for relatively large temporal gaps (time steps of several hours), but compared to drifting buoys the displacement field is spatially much denser. Different parameters used to quantify ice deformation are obtained from the displacement field.

### 4.2 Correlation For Estimation of Ice Displacement

In the following section, we briefly describe the fundamentals of the sea ice motion tracking algorithm developed during the course of the SIDARUS project.

Sea ice drift is estimated using a pattern-based cascaded motion-tracking algorithm initially developed by Thomas [2008] and adapted by Hollands [2012]. The algorithm iteratively calculates the displacement field as follows.

Initially, a resolution pyramid is generated from the input images. In a first step of the displacement calculation, a low-resolution motion field is estimated from a low-resolution set of images, serving as a first guess for the drift vectors. The next step uses a refined resolution of the image pair to analyze more detailed patterns. At each step in the resolution pyramid, the displacement field is initialized using the field estimated during the previous step, and the algorithm searches in a predefined direction. The refined displacement is calculated incrementally in this way during the following steps, until the highest image resolution is reached. Then, the resolution of the displacement field is doubled and initialized with the results from the previous cascade step. The refined displacement field is again iterated over the image pyramid, and those steps are repeated until the highest resolution of both the image pair and the displacement field is reached.

Image intensity patterns are matched using a combination of two different methods: a phase correlation approach to identify patterns in the Fourier domain, and the calculation of the normalized cross-correlation coefficient to select the best match.

$$PC(u,v) = F^{-1} \left[ \frac{F(h) \cdot F^*(g)}{|F(h) \cdot F^*(g)|} \right] \quad (1)$$

The phase correlation (PC) approach, as shown in equation (4.2), was adapted from Canty [2007]. *PC*

is the normalized cross-power spectrum calculated from the Fourier transform  $F(h)$  of the image template  $h$  from the second image shifted by  $(u,v)$  and the complex conjugate of the Fourier transform  $F^*(g)$  of template  $g$  from the first image. The phase correlation has been found to be quite robust in the presence of variations of illumination or offsets in the average image intensity [Foroosh et al, 2002], but on the other hand it is sensitive to additive high-frequency noise [Eckstein and Vlachos, 2009; Manduchi and Mian, 1993].

In the ideal case, the phase correlation displays a sharp peak at the position of the spatial offset of both templates. Under certain conditions, the phase correlation function can display multiple maxima. This can be caused, for instance, if a stationary shelf ice edge and drifting sea ice are present within the image templates. To avoid ambiguities caused by the presence of multiple maxima in the phase correlation function, we follow the approach introduced by Thomas [2008] and estimate the “correct” displacement using a normalized cross-correlation coefficient ( $NCC$ , equation (4.3)) for a set of displacement candidates.

$$NCC_{x,y}(u,v) = \frac{\sum_{j,k=0}^N [h_{u,v}(x_k, y_j) - \bar{h}_{u,v}] \cdot [g(x_k, y_j) - \bar{g}]}{\sqrt{\sum_{j,k=0}^N [h_{u,v}(x_k, y_j) - \bar{h}_{u,v}]^2 \cdot [g(x_k, y_j) - \bar{g}]^2}} \quad (2)$$

Here,  $\bar{h}$  and  $\bar{g}$  are the mean intensities of the templates  $h$  and  $g$ , respectively. The candidates for  $NCC$  calculation are the largest 25% of the PC peaks. By combining both approaches, a more stable result can be achieved since the  $NCC$  is more robust in the presence of noise [Lewis, 1995]. Since it cannot be calculated in the spatial domain, it is numerically less efficient than the phase correlation.

Due to pattern mismatches, spurious displacement vectors can appear at each resolution or cascade step due to false pattern matches. We assume drift patterns to be smooth in the sense that neighboring drift vectors have similar directions and magnitudes. Under this assumption, we remove outliers using a median filter after each iteration. Using the same assumption, we fill small gaps in the drift field caused by pattern loss within the template. The resulting displacement field estimated using this procedure has a resolution of approximately  $1/10^{\text{th}}$  of the original SAR image resolution.

### 4.3 Deformation

We can estimate the deformation of sea ice from the resulting velocity field [Leppäranta, 2011]. Here, the velocity gradient tensor  $u$  is decomposed into strain rate tensor  $\dot{\epsilon}$  and vorticity tensor  $\dot{\omega}$ :

$$u = \dot{\epsilon} + \dot{\omega} = \begin{pmatrix} \frac{\partial u}{\partial x} & \frac{\partial u}{\partial y} \\ \frac{\partial v}{\partial x} & \frac{\partial v}{\partial y} \end{pmatrix} \quad (3)$$

The first invariant of  $\dot{\epsilon}$  is the velocity divergence  $d$ , which can be interpreted as the strain rate along the  $x$  and  $y$  axes:

$$d = \frac{\partial u}{\partial x} + \frac{\partial v}{\partial y} \quad (4)$$

The second invariant is the shear  $s$ , which contains the off-diagonal elements of  $\dot{\epsilon}$  :

$$s = \sqrt{\left(\frac{\partial u}{\partial x} - \frac{\partial v}{\partial y}\right)^2 + \left(\frac{\partial u}{\partial y} + \frac{\partial v}{\partial x}\right)^2} \quad (5)$$

If different velocities act on single field elements, a rotation of the field can be the result. This is described by the invariant of  $\dot{\omega}$ , the vorticity  $v$ :

$$v = \frac{\partial v}{\partial x} - \frac{\partial u}{\partial y} \quad (6)$$

Total deformation is defined as  $\tau = \sqrt{2} \cdot |\dot{\epsilon}|$  :

$$\tau = \sqrt{\underbrace{\left(\frac{\partial u}{\partial x} - \frac{\partial v}{\partial y}\right)^2 + \left(\frac{\partial u}{\partial y} + \frac{\partial v}{\partial x}\right)^2}_{s^2} + \underbrace{\left(\frac{\partial u}{\partial x} + \frac{\partial v}{\partial y}\right)^2}_{d^2}} \quad (7)$$

Parameters derived from the velocity field contain only information about deformation processes taking place in the time between image acquisitions. It is not possible to make assumptions of the general deformation state of the sea ice based on the derived data.

#### 4.4 Quality Assessment

Errors in the derived displacement field can have different sources, such as

- very low backscatter intensity variations in the radar images, which can be sometimes found in relatively featureless new ice areas
- pattern mismatches caused by a highly dynamic ice structure (areas of deformation or new ice production in polynyas)
- pattern loss at the image borders
- spurious displacement vectors occurring if the search windows contain only noise
- a false initial displacement causing the algorithm to search in the wrong direction

A quantitative analysis of the derived drift product cannot be conducted based on the correlation coefficient alone [Hollands et al., manuscript in preparation]. Therefore, the reliability of the displacement field is estimated from a combination of six different statistical and texture-based parameters. For each iteration of the displacement field calculation, those parameters are evaluated for each template pair. In this way, we obtain a quality estimate to accompany every displacement vector.

The most intuitive procedure would be to directly exclude displacement vectors based on those statistics, but we found that this decreases the quality of the resulting displacement field if too many vectors are excluded during runtime. Instead, we set a threshold based on empirical observations for

each of the six parameters. If this threshold is exceeded, we increment a counter value for the corresponding displacement vector. The counter is then, together with the displacement, inherited by the next iteration step.

At the end of the displacement field calculation, we have an error score for each displacement vector. This score needs to be normalized by the number of displacement vector iteration steps, since those are not evenly distributed (for instance, at the image margins, the number of iteration steps is lower than in the center of the image). The result is a normalized error score, or confidence factor (CFA).

An example for the resulting CFA score is shown in the left panel of Fig. 4.1. Here, we can discern different regions. The ice shelf has large CFA values because of the lack of texture. At the center of the image the CFA assumes low values since there is sufficient texture available. Based on the analysis of our data, we set a threshold to define reliable regions at CFA values below 2 (Fig. 4.1, right panel).

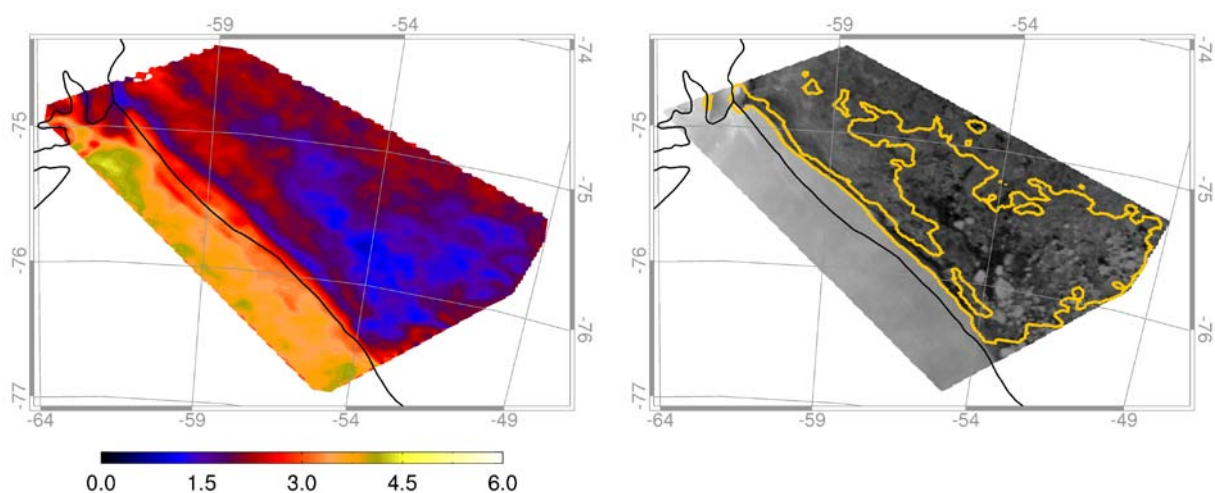


**Figure 4.1: Quality maps for an Envisat ASAR image pair of the Ronne polynia. Images were acquired on 2008/02/19 and 2008/02/20. Left: CFA; Right: result of thresholding at CFA=2**

Another way to validate the quality of the motion tracking result in the absence of reference data is a simple consistency check called backmatching [e.g. Schreer, 2005]. Here, the displacement field is calculated twice, with an interchanged image sequence. In regions where the algorithm makes “bad guesses” due to insufficient texture, the results from both runs are inconsistent. This method is able to identify those highly textured but very dynamic regions the CFA cannot discern. Examples for such regions are found, for instance, in polynias and the ice margin zone.

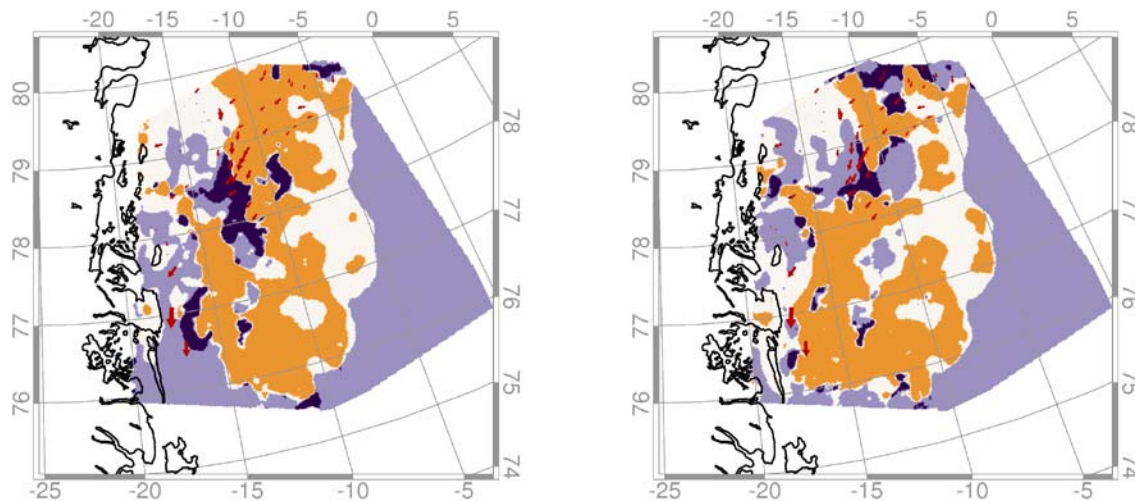


**Figure 4.2: Quality maps for the motion field derived from a pair of Radarsat-2 images acquired on 2012/09/16. Left: HH polarization; Right: HV polarization.**

Fig. 4.2 shows displacement fields calculated from a Radarsat-2 image pair recorded on the 16.09.2012 with  $\approx 10$ h time difference between image acquisitions. The map on the left shows the displacement field estimated from HH polarization, and the image on the right shows the result from the HV-polarized data. The red arrows are visually determined reference data. From a comparison between backmatching and texture analysis, we can discern the following regions:

- ① In this region, displacement vectors are marked as reliable by both approaches.
- ② This region is marked as unreliable by both the texture-based approach and backmatching. In the example above, this is mostly open water, but also homogeneous-looking areas
- ③ Here, the texture-based approach considers an area to be reliable which is found to be inconsistent by backmatching. This happens, for instance, at the ice margin zone with its fast-changing ice conditions.
- ④ Regions that fall into this class are considered reliable by backmatching, but fail the texture-based quality criterion.

It can be seen in Fig. 4.2 that there are slightly different regions marked as reliable, depending on polarization. The displacement field calculated from HH-polarized SAR images shows fewer gaps than the result obtained from cross-polarized data. It has been indicated that both channels are sensitive to different structures in the ice and hence contain complementary information [Komarov, 2012], and our own analysis supports this finding.

## 4.5 Technical Overview

During the past project phase, we made some changes to our drift detection algorithm. The major part consisted of a partial re-implementation in C in order to reduce runtime and increase portability for users. We also improved the error handling and the user interface, which is an important factor for the applicability in an operational context.

In accordance with user requirements, our toolbox is now capable of producing NetCDF output files, which adhere to the CF1.6 standard. In order to integrate into the SAR image processing chain of end users, we changed the structure of our data input procedures. The software can now read a pair of geotiff input files and automatically select the overlapping regions.

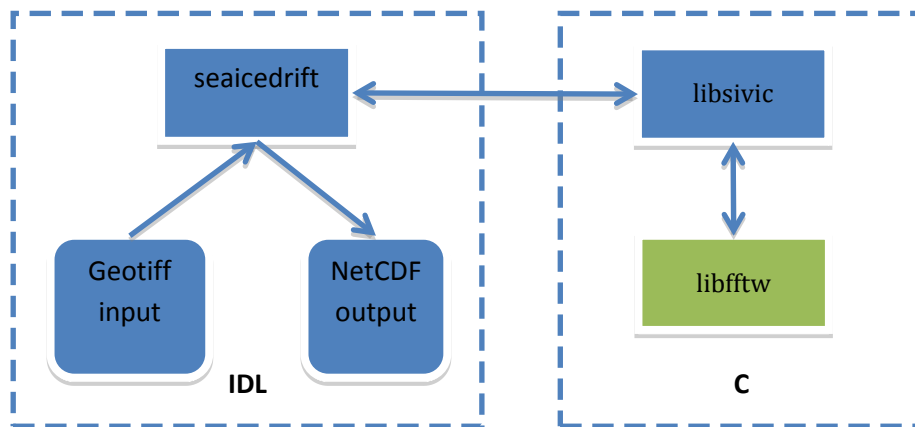


**Figure 4.3: Architecture of the sea ice drift detection toolbox. Libraries “libsivic” and “libfftw are written in C.**

Fig. 4.3 shows the layout of the drift detection toolbox. We implemented the user interface, file I/O and geocoding in the sea ice drift module, which is currently available as an IDL save-file. From this module, we call an external library (libsivic), which is written in C and contains the numerically demanding parts of the code. Data exchange between both worlds is handled by IDL’s CALL\_EXTERNAL() routine. In libsivic, we use an external library (libfftw version 3.3.3) to compute the phase correlation for our motion detection routine. Libfftw is an open source software project and is licensed under the GPL. It is available from <http://www.fftw.org>.

Additionally, users are provided with an extensive technical documentation in HTML/PDF format.

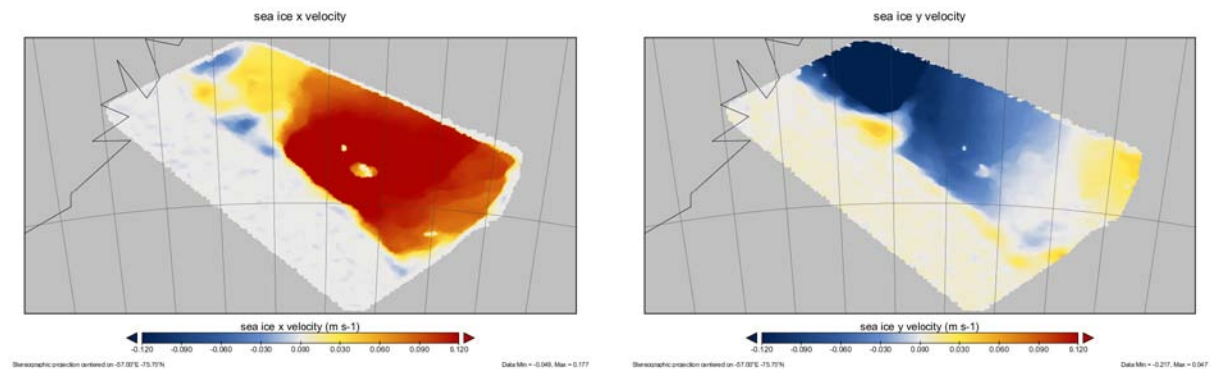
## 4.6 Results/Products

In this section we will show examples of the products our toolbox generates. The drift product is organized as follows:

<i>parameter / NetCDF variable</i>	<i>variable type</i>	<i>Unit</i>
direction_of_sea_ice_velocity	Float	Degrees
sea_ice_divergence	Float	s <sup>-1</sup>
sea_ice_drift_reliability_flag	byte	-
sea_ice_shear	float	s <sup>-1</sup>
sea_ice_speed	float	m·s <sup>-1</sup>
sea_ice_total_deformation	float	s <sup>-1</sup>
sea_ice_vorticity	float	s <sup>-1</sup>
sea_ice_x_velocity	float	m·s <sup>-1</sup>
sea_ice_y_velocity	float	m·s <sup>-1</sup>

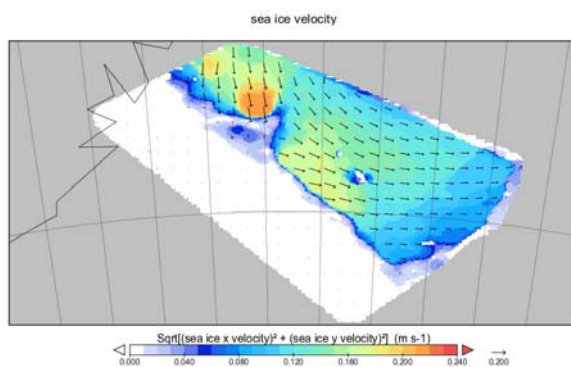
#### 4.6.1 Sea ice velocities

Fig. 4.4 shows the main product generated from our software: sea ice velocities calculated from a pair of spatially overlapping SAR images. The left panel shows the sea ice velocity component in x direction; the right panel shows the velocity component in y direction.



**Figure 4.4: Sea ice drift parameters from the NetCDF output files. Drift field generated from an Envisat ASAR image pair acquired on 2008/02/22 and 2008/02/23.**

Sea ice velocity magnitude and drift direction can also be displayed based on the output data. An example is shown in Fig. 4.5.



**Figure 4.5: Sea ice speed and direction. Drift field generated from an Envisat ASAR image pair acquired on 2008/02/22 and 2008/02/23.**

#### 4.6.2 Drift vector reliability charts

A supplementary dataset is the classification of the ice drift retrieval results into reliable and unreliable vectors. Users can choose between an evaluation based on texture analysis or based on backmatching. The resulting binary mask is provided in the output as a separate NetCDF layer.

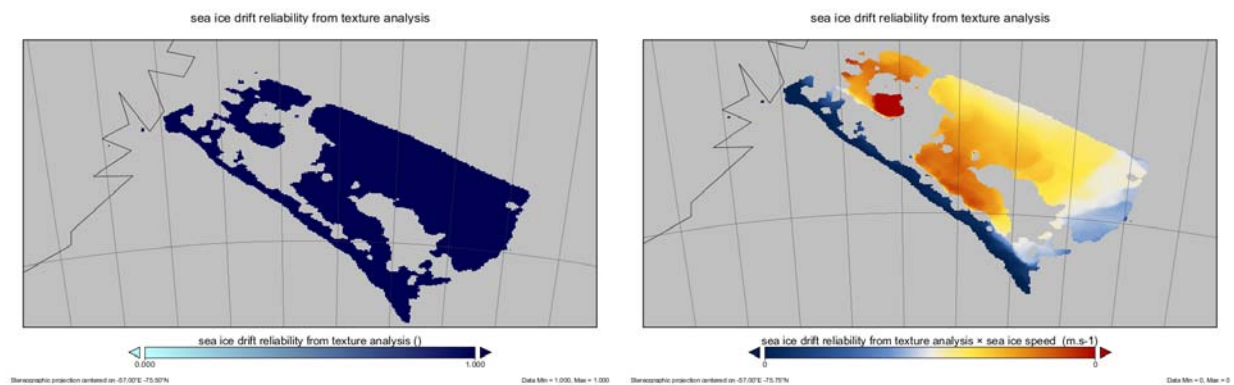


**Figure 4.6: Left: Reliability mask based on texture analysis; Right: Sea ice speed combined with binary mask. Data set: Envisat ASAR image pair recorded on 2008/02/22 and 2008/02/23.**

#### 4.6.3 Sea ice deformation determined from the displacement field

Sea ice deformation is calculated from the drift field using equations (3) – (7). The left panel of Fig. 6 shows a map of the divergence calculated from the displacement field. Here, green are zones of divergence, and blue zones are convergent regions. In the right panel of Fig. 6, the vorticity of the derived velocity field is shown. Red and yellow areas rotate in anticlockwise direction, while blue areas rotate clockwise.

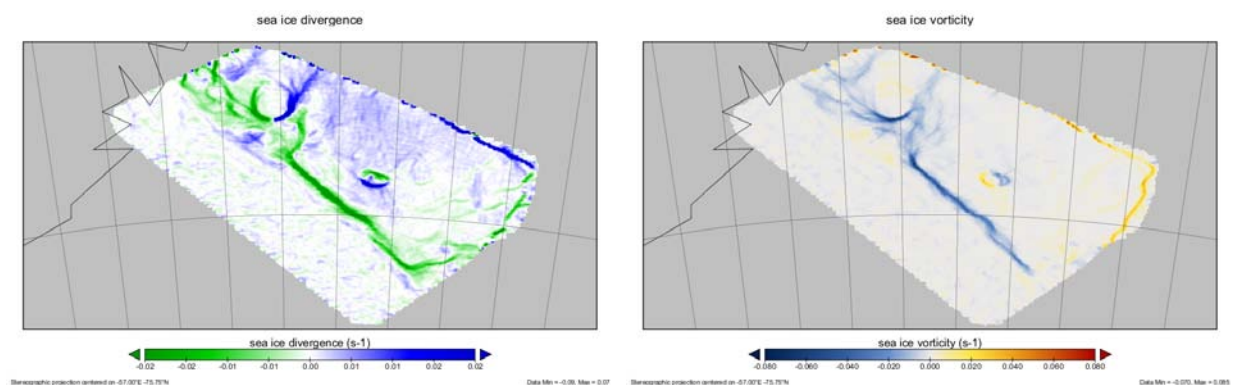


**Figure 4.6: Left: Divergence map derived from Envisat ASAR image pair recorded on 2008/02/22 and 2008/02/23; Right: Vorticity map from the same data set.**

## 4.7 References

Canty, M. J., *Image analysis, Classification and Change Detection in Remote Sensing: With Algorithms for Envi/IDL*, CRC/Taylor & Franics, 348 pp., ISBN: 0-8493-7251-8

Eckstein, A. and Vlachos, P. P., *Digital particle image velocimetry (DPIV) robust phase correlation*, Measurement Science and Technology, 20, 5, 2009, p.15, doi:10.1088/0957-0233/20/5/055401

Fily, M and Rothrock, D. A., *Sea ice tracking by nested correlations*, IEEE Transactions on Geoscience and Remote Sensing, vol. GE-25, no. 5, pp. 570-580, 9 1987.

Foroosh, H. et al., *Extension of Phase Correlation to Subpixel Registration*, IEEE Transactions on Image Processing, 11, 2002, pp. 188-200, doi:10.1109/83.988953

Hollands, T., *Motion tracking of sea ice with SAR satellite data*, PhD Thesis, Bremen University, 2012

Komarov, A. and Barber, D., *Detection of sea ice motion from co- and cross-polarized RADARSAT-2 images*, Geoscience and Remote Sensing Symposium (IGARSS), 2012 IEEE International, 2012, 3277-3280

Kwok, R. et al., *An ice-motion tracking system at the Alaska SAR facility*, IEEE Journal of Oceanic Engineering, vol. 15, no. 1, pp. 44-54, 1, 1990.

Jenkin, M. R. et al., *Techniques for disparity measurement*, CVGIP: Image Understanding, vol. 53, no. 1, pp. 14-30, 1, 1991.

Leppäranta, M., *The Drift of Sea Ice*, ed. by P. Blondel, 2nd ed., Springer – Praxis books in Geophysical Sciences, Springer, Berlin/Heidelberg, 347 pp. ISBN: 978-3-642-04693-4, doi:10.1007/978-3-642-04683-4

Lewis, J. P., *Fast Normalized Cross-Correlation*, in Proceedings of Vision Interface 95, Quebec City, Canada, pp. 120-123

Manduci, R. and Mian, G. A., *Accuracy Analysis of Correlation-Based Image Registration Algorithms*, in IEEE International Symposium on Circuits and Systems (ISCAS), IEEE, Chicago, IL, pp. 834-837, doi:10.1109/ISCAS.1993.393852

Pan, B. et al., *Mean intensity gradient: An effective global parameter for quality assessment of the speckle patterns used in digital image correlation*, Optics and Lasers in engineering, vol. 48, no. 4, pp. 469-477, 4 2010.

Pearlstine, L. et al., *Textural discrimination of an invasive plant, schinus terebinthifolius, from low altitude aerial digital imagery*, Photogrammetric Engineering & Remote Sensing, vol. 71, no. 3, pp. 289-298, 3 2005.

Schreer, O., *Stereoanalyse und Bildsynthese*. Springer, 2005.

Shavit, U. et al., *Intensity Capping: a simple method to improve cross-correlation PIV results*, Experiments in Fluids, 2007, 42, 225-240

Thomas, M., *Analysis of Large Magnitude Discontinuous Non-rigid Motion*, PhD Thesis, University of Delaware, 2008

**END OF DOCUMENT**